ADVANCED OPTICAL MATERIALS
www.advopticalmat.de

Low-Frequency Phonon Modes in Layered Silver-Bismuth Double Perovskites: Symmetry, Polarity, and Relation to Phase Transitions

Beatriz Martín-García, Davide Spirito,* Miao-Ling Lin, Yu-Chen Leng, Sergey Artyukhin, Ping-Heng Tan, and Roman Krahne**

Metal-halide perovskites (PSKs) are emergent materials for a large range of applications, and the layered double PSK architectures vastly enrich the opportunities to design their composition, structural properties, and optoelectronic behavior. The stability, crystal phase, and electronic bandgap depend strongly on the bonds and distortions of the octahedra lattice that are at the origin of the vibrational spectrum of these materials. This work investigates the structural dynamics of flakes of exfoliated layered Ag-Bi bromide double PSKs by angle-dependent polarized Raman spectroscopy and density functional theory modeling. The well-defined orientation of the inorganic octahedra lattice with respect to the light polarization allows to correlate the angle-dependent intensity of the Raman signal to the directionality and symmetry of the phonon modes. Low-frequency vibrations are revealed for which a detailed microscopic and group theory assignment of the Raman modes is provided. The temperature-dependent measurements across the phase transitions show marked changes in the phonon frequencies, reveal soft modes, and help to distinguish first from second-order transitions as well as to determine their transition temperature. This provides highly valuable insights to improve the properties of this class of Pb-free PSKs for applications in energy harvesting and optoelectronics.

1. Introduction

Metal-halide double perovskites (PSKs) are receiving an increasing attention as more environmentally friendly and stable alternatives to the Pb-based PSKs.[1] Although they do not yet reach the high performance of their Pb counterparts in optoelectronic devices, recent efforts, particularly on $Cs_2AgBiBr_6$ double PSKs,[2] demonstrate their potential use in a broad range of applications from solar cells,[3–9] photodetectors,[10,11] X-ray detectors,[12] memristors[13] to photocatalysts.[14] Moreover, when passing from the 3D double PSK toward its layered counterparts with two (2L) or one (1L) octahedra layers by introducing large A-site organic cations, such as butylammonium (BA) or propylammonium (PA), allowed to develop new two-dimensional (2D) materials with tunable optoelectronic properties, such as the character of the bandgap as well as the bandgap energy from ≈ 2 eV to ≈ 3 eV, which is related to the distortion of the inorganic lattice.[15–19] The dimensional reduction also improved remarkably the ON/OFF ratio of memristors from 10^2 ($Cs_2AgBiBr_6$—3D) up to 10^7 ($(BA)_2CsAgBiBr_7$), since in distorted crystal structures the ion migration is favored.[20] X-ray photodetectors from $(BA)_2CsAgBiBr_7$ with large mobility-lifetime product were obtained, where the sensitivity depends on the dimensionality of the crystal (number of octahedral layers).[21,22] The time response of photodetectors could be enhanced through dimensional reduction, while keeping a similar detectivity;[23]

B. Martín-García
CIC nanoGUNE BRTA
Tolosa Hiribidea, 76, Donostia-San Sebastian
Basque Country 20018, Spain
E-mail: b.martingarcia@nanogune.eu

D. Spirito
IHP–Leibniz-Institut für innovative Mikroelektronik
Im Technologiepark 25, 15236 Frankfurt (Oder), Germany
E-mail: spirito@ihp-microelectronics.com

The ORCID identification number(s) for the author(s) of this article can be found under https://doi.org/10.1002/adom.202200240.

DOI: 10.1002/adom.202200240

M.-L. Lin, Y.-C. Leng, P.-H. Tan
State Key Laboratory of Superlattices and Microstructures
Institute of Semiconductors
Chinese Academy of Sciences
Beijing 100083, China

M.-L. Lin, Y.-C. Leng, P.-H. Tan
Center of Materials Science and Optoelectronics Engineering & CAS
Center of Excellence in Topological Quantum Computation
University of Chinese Academy of Sciences
Beijing 100190, China

S. Artyukhin, R. Krahne
Istituto Italiano di Tecnologia
Via Morego 30, Genova 16163, Italy
E-mail: roman.krahne@iit.it

and in $(PA)_2CsAgBiBr_7$ its layered structure leads also to strong polarization sensitivity.[24] The examples above demonstrate that the crystal structure determines the bandgap, exciton binding energy, density of trap states, and more, and therefore governs the optoelectronic properties, emphasizing the need of a detailed study of the structural dynamics. While the optical properties were extensively studied, showing indirect bandgap and large electron–phonon coupling strength in 3D $Cs_2AgBiBr_6$,[25–31] the structural dynamics have received less attention.[25,26,30,32] This is even more true for the structural dynamics in layered Ag/Bi-based double PSKs, for which we studied the high-frequency modes by Raman spectroscopy in a previous work, evidencing the impact of the organic cations in phase transitions.[33] However, for the optoelectronic properties, the vibrational modes of the inorganic PSK lattice in the low-frequency range are particularly relevant, as has been demonstrated for 3D[34–38] and layered[39–43] PSKs, and the properties of these vibrational modes have not been studied in the double PSKs so far.

In this work, we investigate the vibrational properties of a family of Ag/Bi double PSKs comprising 3D bulk crystals and the layered structures with one (1L) and two (2L) inorganic metal-halide layers. Angle-dependent polarized Raman spectroscopy enables a detailed analysis of the symmetries of the basic phonon modes, which is combined with symmetry assignment by group theory and insight on the vibrational motions by density functional theory (DFT) modeling. This allows to distinguish modes with "isotropic," "dipolar," and "quadrupolar" features in their angular dependence, and to assign them to vibrations of the octahedra cages, the inorganic metal-halide lattice bonds, and/or coupling to the organic cations in the case of the 1L and 2L structures. We focus our study on the low-frequency range of 8–200 cm^{-1} where the phonon bands of the inorganic lattice are located, and present the detailed Raman mode spectrum for the 3D, 2L, and 1L Ag/Bi double PSKs for both their room temperature (RT, taken as 300 K) and low temperature phases. Our access to the ultralow-frequency range allowed us to reveal two bands in the 3D structure that have not been reported before, appearing at ≈ 18 and ≈ 29 cm^{-1} in the low-temperature tetragonal phase. Concerning the 1L and 2L structures, we present the first study of the low-frequency Raman bands (below 80 cm^{-1}), where we identify a wealth of Raman-active bands that can be related to octahedra motions and metal–Br bond stretching or bending. Interestingly, we find some soft modes that appear only in the low-temperature phase and for which their frequency decreases markedly with increasing temperature. Mapping the temperature behavior and the symmetry of the phonon modes allows to clearly identify the phase transition temperature in our samples, and provides additional insights if the phase transition consists of a first-order process involving structural changes of the inorganic lattice, or second-order processes that stem from order/disorder transitions in the organic layers.

2. Results and Discussion

Figure 1 shows optical microscope images of the double PSK crystals that are investigated by Raman spectroscopy and DFT modeling in this work, together with cross-section views of their crystal structure illustrating their room and low-temperature phases. The 3D crystals grow forming a truncated cube (Figure 1 and Figure S1, Supporting Information), providing optical access to their {111} facets as flat surface, and are in cubic phase at RT and tetragonal phase below 120 K.[26] For the low-dimensional layered structures we mechanically exfoliated single flakes with the (001) plane parallel to the SiO_2/Si substrate surface. For the 2L-BA and 1L-BA layered samples the structure is monoclinic both at RT and low temperature. However, in the range 100–298 K for 2L-BA[15] and ≈ 282 K for 1L-BA[33] there is a conformational order to disorder rearrangement of the organic cations accompanied by a change in the octahedral tilting (angle and bonds distortion) inside the inorganic lattice (Figure 1b,c), leading to a phase transition of the whole crystal structure. The optical and structural properties (temperature-dependent absorption and photoluminescence and X-ray diffraction (XRD)) of the crystals were reported in ref. [33].

Figure 2 shows unpolarized Raman spectra recorded at room temperature and 30 K for all samples, thus above and below the phase transitions, together with the results from DFT modeling of the Raman-active modes at 0 K. For all three double PSK structures, the room temperature Raman spectra are dominated by a high-frequency mode around 170 cm^{-1}, that is slightly red-shifted in the layered structures by reducing the number of octahedral layers, in agreement with the literature.[33] Furthermore, a strong mode at 73 cm^{-1} is observed in the 3D sample, while the 2L and 1L structures show multiple peaks in the low-frequency range below 100 cm^{-1}. The low-temperature Raman spectra reveal a much more complex response, with different sets of phonon modes in the low-frequency regime. This marked difference between room and low-temperature spectra can be attributed to the crystal phase transition (at 122, 100–298, and 282 K for 3D,[26] 2L,[15] and 1L[33] structures, respectively), and because of the drastically reduced thermal noise and broadening at low temperatures that allow to resolve weak and narrow phonon bands. The low-temperature Raman spectra can be compared with DFT modeling at 0 K (see details in Section S2, Supporting Information), where the Raman-active modes (stemming from optical phonons), their symmetry, and their relative intensities are shown in the bottom row of Figure 2. Furthermore, in the DFT modeling a depolarization factor D can be defined as the ratio of the polarized (∥) and depolarized (⊥) intensities averaged over the incidence angle. This D can be assigned to the vibrations of the ionic lattice that allows to classify the modes into "isotropic," "dipolar," and "quadrupolar" ones, as detailed in the caption of Figure 2. We established this notation according to the angle dependence of the Raman modes in the polar plots discussed in detail later (Figures 4–6). We note that passing from 3D to 2D layered compounds leads to a reduction in symmetry of the system, which changes the point group from C_{4h} (for 3D) to C_2 (for 2L-BA) and C_{2h} (for 1L-BA).[15,26] Overall, we find a good agreement between the experimental data and DFT modeling, which allows us to analyze the vibrational motions of the dominant modes in those crystal structures.

The dominant phonon mode around 170 cm^{-1} that is observed in all experimental spectra is isotropic and A_{1g}-like.

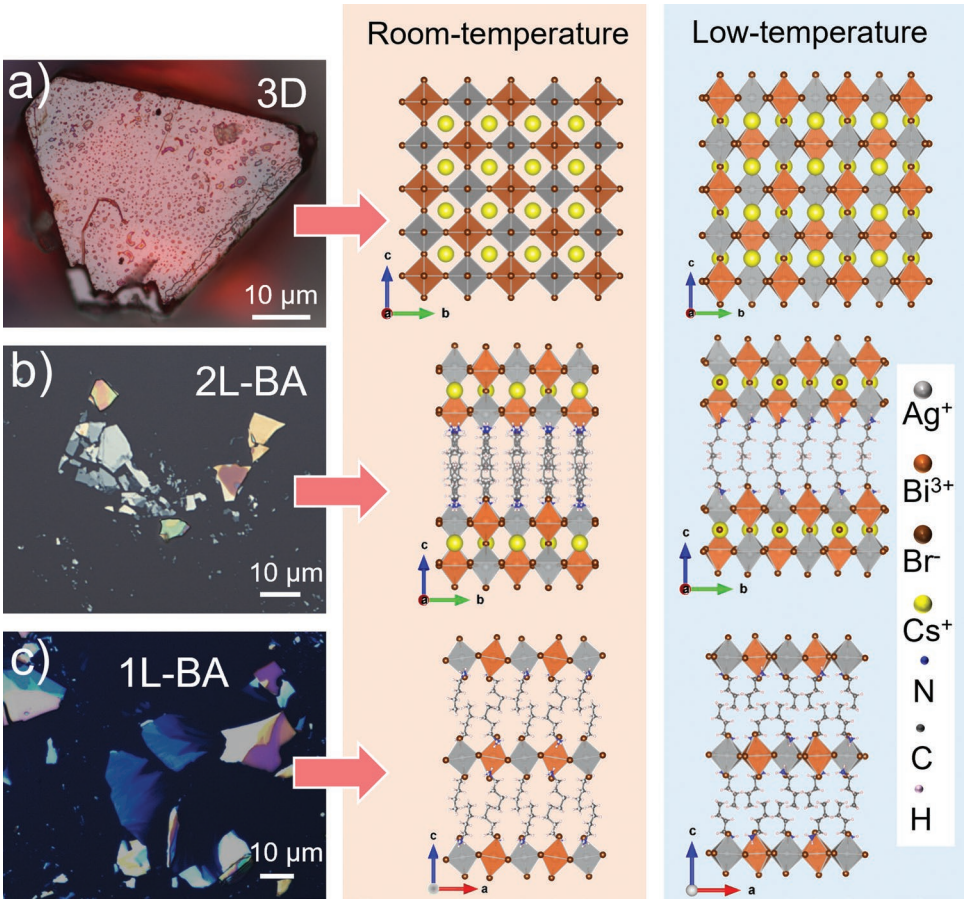

Figure 1. Optical microscope images of the different double perovskite structures: a) 3D $Cs_2AgBiBr_6$ microcrystals, and mechanically exfoliated b) 2L-BA and c) 1L-BA flakes on SiO_2/Si substrates together with their crystal structures drawn using VESTA 3 software[44] based on the crystallographic data from refs. [15,26].

It is typically attributed to the longitudinal-optical (LO) phonon mode and dominated by out-of-plane oscillation components. Then, the 3D crystals have two more pronounced modes around 140 and 75 cm^{-1} that have E_g symmetry.[25,30] Furthermore, we observe at low temperature a set of four peaks at 18, 29, 40, and 45 cm^{-1} that we assign to rocking and/or twisting motions in the $[AgBr_6]^{5-}$ and $[BiBr_6]^{3-}$ octahedra, which is in line with ref. [30] and the interpretation of the lowest energy modes in lead-halide PSKs.[45] The low-frequency range of the 1L-BA and 2L-BA samples features a much larger set of peaks with different symmetries that will be discussed in detail later on.

To get deeper insight into the symmetries of the phonon modes we performed angle-dependent polarized Raman spectroscopy, which allows to correlate the linear polarization in excitation (polarizer) and detection (analyzer) with the orientation of the 2D lattice under investigation. Here the rotation of the linearly polarized light in the combined excitation/detection path (see Experimental Methods in Supporting Information) with a $\lambda/2$ wave plate by an angle of $\theta/2$ is equivalent to the rotation of the sample reference frame by an angle θ to the reference frame of the linear polarizers. Therefore we can interpret the data as if the orientation of the linear polarizers, which are parallel (polarized) or orthogonal (depolarized), is rotated with respect to the sample.[46] Such investigation of the Raman modes with well-defined light polarization with respect to the lattice orientation of the sample provides detailed insight into the underlying symmetries of the phonon bands and the directionality of the vibrations in the ionic octahedra lattice.

However, before we present such analysis in detail for the 2L-BA and 1L-BA structures, we will discuss our angle-dependent Raman results of the 3D crystals, that due to the (111) surface facet does not provide octahedra lattice planes at orthogonal angles to the light polarization or pointing vector.

Figure 3a shows the view on one octahedra lattice plane of the 3D structure from the diagonal direction that corresponds to the exposed (111) surface plane. We note that this geometry does not allow a straightforward assignment of phonon symmetries, because the light polarization is diagonal to the in-plane and out-of-plane components in the octahedra lattice. Nevertheless, we observe an angle dependence of the Raman intensity for some modes, in particular for the low-frequency modes at 18, 29, 40, and 45 cm^{-1} at low temperature in both polarized and depolarized measurements. This illustrates that the relative intensity of Raman-active modes measured from single crystals can strongly depend on the experimental configuration. The other modes that we observe at 73 and 140 cm^{-1} have roughly constant intensity regardless of the

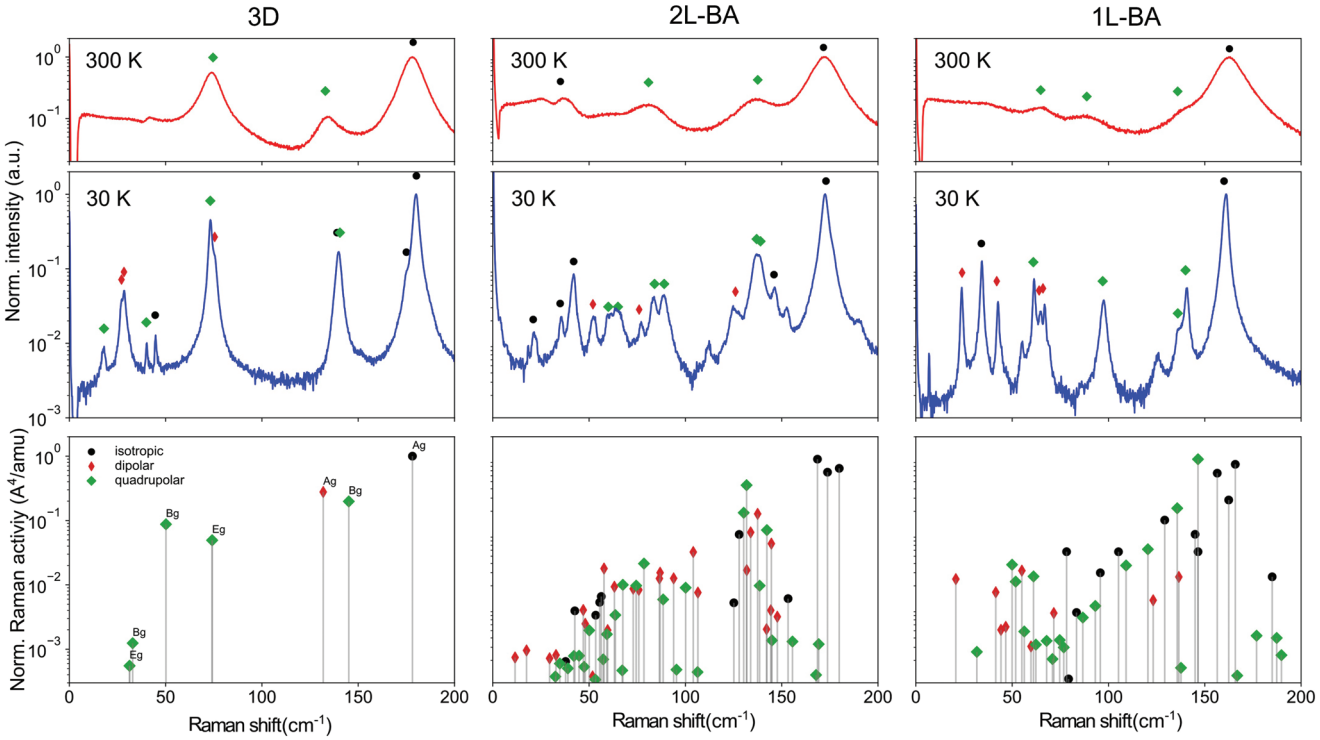

Figure 2. Comparison of the experimental Raman spectra using *y*-axis logarithmic scale for highlighting the low-intensity modes and DFT results for 3D, 2L-BA, and 1L-BA samples. Experimental data are unpolarized spectra measured at RT and 30 K (shown on semi-log scale), normalized to the strongest peak. The DFT modeling results are displayed in terms of Raman frequency and activity. The symbols mark the polarization of the modes that are defined by the depolarization factor *D*, classified as "isotropic" for $D < 0.15$ (black circles), "dipolar" for $0.15 < D < 0.72$ (red diamonds), and "quadrupolar" for $D > 0.72$ (green diamonds).

rotation angle of the polarization, and the LO phonon mode at 180 cm^{-1} manifests an angle dependence only in depolarized measurements. We present a symmetry analysis based on the Raman tensor in such a rotated system in Section S5.2, Supporting Information.

We now turn to the layered double PSKs 2L-BA and 1L-BA structures. Here the exfoliated flakes have their (001) plane parallel to the substrate, and therefore we can straightforwardly relate the angle dependence of the Raman-active modes to the crystal symmetries. For a facile overview of the behavior of the different modes we will use polar plots of the angle-dependent intensity of the different Raman modes. Such a polar plot is sketched in **Scheme 1** together with the fixed orientation of the octahedra lattice, where the angle corresponds to the direction of the light polarization, and the radius to the normalized angle-dependent intensity of the mode.

The intensity of a Raman mode is given by $|\vec{e}_i \overleftrightarrow{R} \vec{e}_s|^2$, $\vec{e}_s$ and $\vec{e}_i$ being the polarization of scattered and incident light, and the Raman tensor $\overleftrightarrow{R}$. As in our experimental configuration, the incidence is along the *z*-axis, and the collected light is polarized in the *xy*-plane. For non-resonant excitation, the Raman tensor is

$$\overleftrightarrow{R} = \begin{pmatrix} a & d & \cdot \\ d & b & \cdot \\ \cdot & \cdot & \cdot \end{pmatrix} \quad (1)$$

where the coefficients related to polarization along *z* are replaced by a dot.

Figure 4a shows the calculated angular dependence of the Raman intensity for different values of *a*, *b*, *d* that result from different symmetries (see Section S5, Supporting Information for details on the calculation). We find an isotropic A_{1g}-like mode for a diagonal Raman tensor with $a = b$. Dipolar (red) and quadrupolar (green/brown) modes are obtained for other combinations of these tensor components, where $d \neq 0$ leads to lobes at diagonal angles. In particular, we can also assign the angular pattern for the quadrupolar E_g- and T_{2g}-like modes.

DFT modeling based on the structural data reported in refs. [15,26] provides atomistic insight to the vibrational motions, as illustrated in Figure 4b. The isotropic A_{1g}-like modes correspond to symmetric stretching of the octahedra. The low-frequency quadrupolar E_g-like modes can be related to asymmetric octahedra stretching, and the T_{2g} modes to Ag–Br or Bi–Br bond bending caused by an orthogonal motion of the Br ions. In the layered 2L-BA and 1L-BA structures, A_{1g}-like and E_g-like modes couple to motions of the organic spacer. The organic molecules bind to the octahedra lattice through hydrogen bonds with the Br ions, which facilitate the coupling of the vibrations of the inorganic lattice to the organic spacers.

Figure 5 shows the color plot of the angle-dependent Raman spectra (recorded at 30 and 300 K) and polar plots for all observed modes of the 2L-BA sample ordered by symmetry and frequency for low and room temperature (see Figure S5, Supporting Information for the additional color plots of the Raman spectra). For the low-temperature monoclinic phase we observe isotropic (A_{1g}-like) character for the three low-frequency

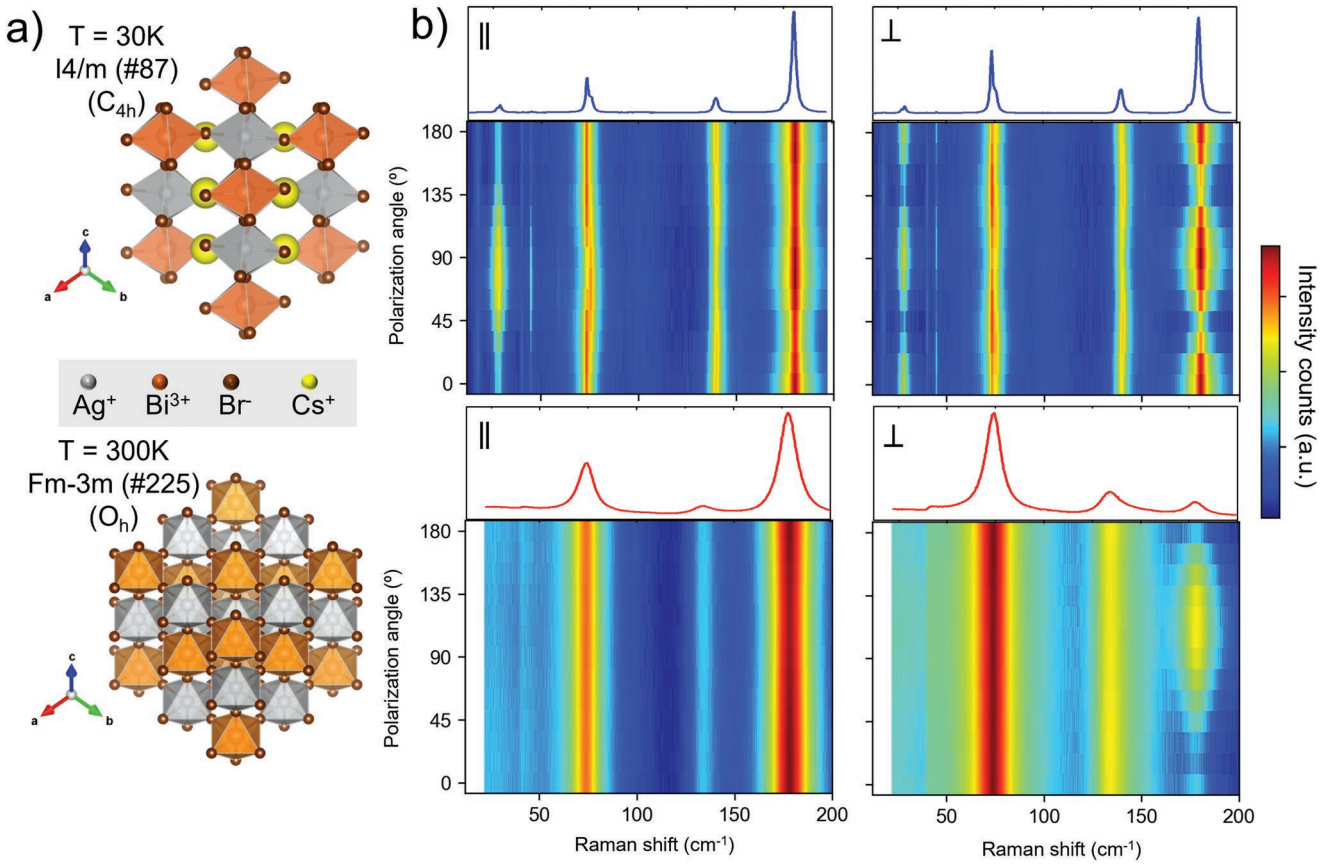

Figure 3. a) Crystal structures of the 3D $Cs_2AgBiBr_6$ PSK drawn using VESTA software[44] for the low- and high-temperature phases[26] from the perspective of the (111) plane that is exposed in the experiment. b) Color plots of the angle dependence of the Raman spectrum for polarized (||) and depolarized (⊥) configurations. The integrated Raman spectra along the polarization angle are shown on top of the color plots.

modes and for the dominant high-frequency modes at 146 and 173 cm^{-1}. The isotropic low-frequency modes result from octahedra stretching that involves the coupled motions of the Br^- ions. The isotropic high-frequency A_{1g}-like modes at 146 and 173 cm^{-1} stem from stretching of the octahedra cages, as evidenced by our DFT calculations (Figure 4b). This is in good agreement with the typical assignment of the strong mode at 173 cm^{-1} as an LO phonon mode with out-of-plane oscillation.[25,30] In the frequency range typical for metal cation–Br bond bending or stretching, from 60 to 140 cm^{-1}, we observe dipolar and quadrupolar modes with different directionality. Quadrupolar modes reflect the bidirectional symmetry of the octahedra lattice, and T_{2g}-like modes are strong along its diagonal directions, while the E_g-like mode is strong along the metal cation–Br bond directions. The E_g-like mode with relatively strong intensity originates from Ag–Br and Bi–Br bond stretching along the horizontal/vertical directions as evidenced by DFT (Figure 4b), which is also agrees with the direction of those bonds in the crystal structure in Figure 5b.

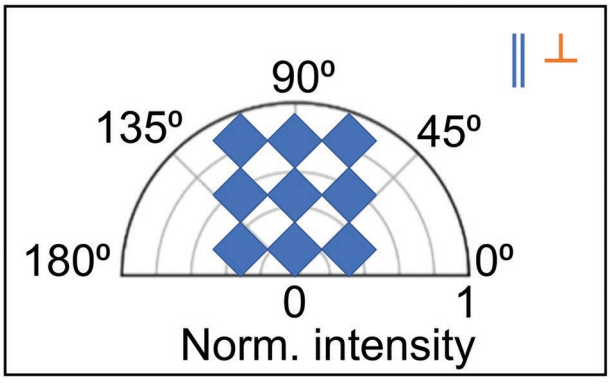

Scheme 1. Polar plot scheme where the angle gives the direction of the light polarization with respect to the fixed frame of the octahedra lattice (sketched by the array of blue squares) of the sample. The normalized mode intensity is given by the length of the radial coordinate.

The directionality of the T_{2g}-like modes corresponds to the axes of the Cs-ion sublattice; however, the T_{2g}-like modes involve also Ag–Br or Bi–Br bond bending as evidenced by our DFT modeling. The appearance of multiple modes should then result from different coupling between the sublattices.

The dipolar modes are induced by the preferential orientation of the organic molecules in the low-temperature phase along one direction.[33] The butylammonium cations bind to the Br ions in the inorganic octahedra lattice via hydrogen bonds,[47] which can induced static distortions, and facilitates coupling of the inorganic lattice modes to the organic molecules. Above the phase transition at RT the orientation of the molecules is changed and no dipolar modes are observed. The quadrupolar

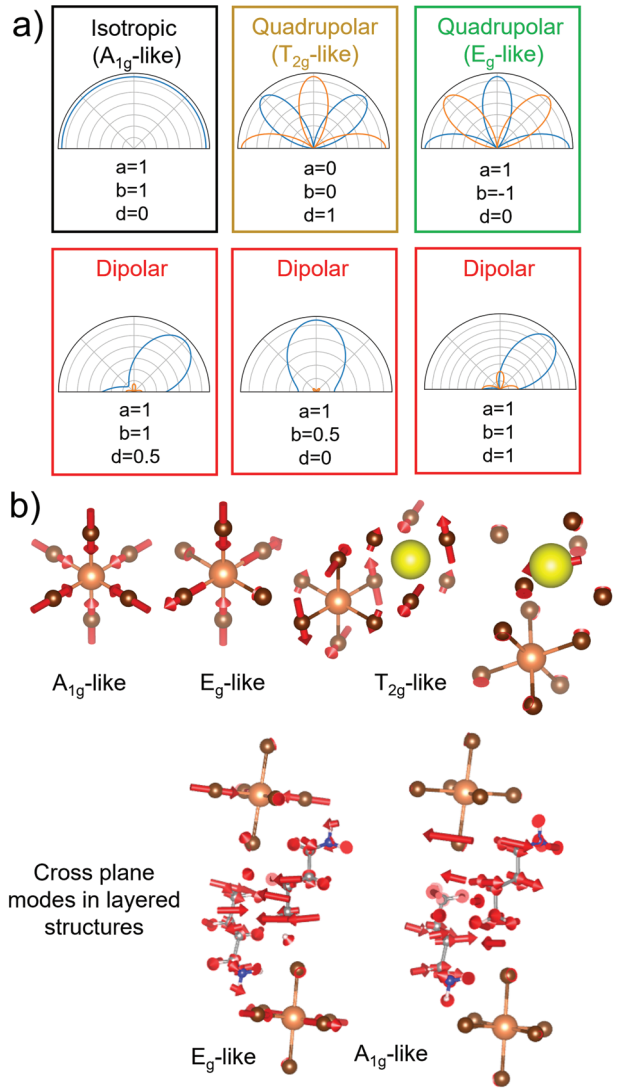

Figure 4. a) Polar plots of the Raman mode calculated from the Raman tensor for selected values for its components. b) Vibrational motions of the different modes obtained by DFT modeling (only the sketches of the atoms involved in the main Raman modes are shown, see Supporting Information for the description of the rest of modes).

mode at 136 cm^{-1} maintains its E_g-like behavior at RT, evidencing that the crystallographic axis directions are not altered by the phase transition, in agreement with the interpretation that this phase transition is triggered by rearrangement of the organics.

Figure 6 shows the angular properties of the phonons in the 1L-BA sample. In the 1L-BA crystal structure at low temperature we notice a strong distortion of the in-plane angles, similar to the lead-halide counterpart,[47,48] which is lifted at RT, where the in-plane angles are again close to 90°. In contrast to the 2L-BA sample where the low-frequency modes were isotropic, here the modes at 24 and 42 cm^{-1} at low temperature are dipolar, which we attribute to the in-plane distortion of the octahedra lattice that affects the vibrations of the octahedra. Then at 64 and 66 cm^{-1}, two more dipolar modes are observed that should stem from bond stretching in the inorganic lattice affected by the organic molecules, as discussed for the 2L-BA sample.

Two isotropic modes are identified: one at low frequency similar to the 2L-BA sample, and one high-frequency mode that results from out-of-plane oscillations and resembles the LO phonon mode. Furthermore, we observe four quadrupolar E_g-like modes that should originate from in-plane bond stretching, as in the other samples. The large number of the E_g-like modes can be associated to the distorted in-plane lattice.

Interestingly, we do not observe dominant T_{2g}-like modes in the 1L-BA sample, which strengthens our interpretation that these modes are related to the Cs-ion sublattice. And at RT we do not observe any dipolar modes, which is caused by the phase transition that leads to a disordered (liquid-like) phase of the organic cations, and almost orthogonal in-plane angles in the inorganic lattice.

Finally, we discuss the temperature-dependent behavior of the Raman modes displayed in **Table 1**. As shown in **Figure 7**, for the 3D structure, we determine the phase transition temperature from tetragonal to cubic at 110–150 K, in good agreement with the 122 K obtained by XRD, absorbance and heat capacity results reported in the literature.[26] This is most evident for the dipolar low-frequency mode that red-shifts with increasing temperature toward the phase transition, and finally quenches at the transition temperature. This is the behavior of a soft mode. Similarly, for the 2L-BA sample, we find a phase transition temperature of ≈ 200 K (Figure 7) from the dependence of the T_{2g}-like mode at 90 cm^{-1} that also is not present above the phase transition temperature. This transition was still not established in the literature, although expected from XRD results in the range 100–300 K.[15] In the 1L-BA case, the transition is clearly marked by an abrupt shift of the mode frequencies at 282 K, in accordance with our previous results for the modes at 140 and 160 cm^{-1}.[33] We note that the mode at 90 cm^{-1} changes character at the phase transition, from E_g-like feature at low temperature to T_{2g}-like feature at high temperature, and that this transition leads to a decrease in frequency, while for all other modes the transition to the high-temperature phase leads to a blue-shift.

The fact that we observe gradual or abrupt changes of the frequencies of certain Raman modes at the phase transition allows us to distinguish first- and second-order phase transitions. The discontinuous change in frequency of the A_{1g} mode at 160 cm^{-1} and E_g mode at 60 cm^{-1} in the 1L-BA sample clearly identifies a first-order phase transition, where the crystal lattice changes configuration. This is in agreement with the XRD results[15] from which Figure 1 was derived. The continuous change in frequency of the A_{1g}-like and other modes in the 2L-BA and 3D sample point to a second-order transition, where only the organic molecule conformation changes from an ordered to a disordered phase.

In conclusion, we presented a comprehensive study of the Raman-active vibrational modes in double PSKs with Ag and Bi as metal cations, including DFT modeling and point group symmetries. We demonstrated that angle-dependent polarized Raman spectroscopy is a versatile tool to experimentally access the directionality and symmetry of the fundamental phonon modes of the (low-dimensional layered) PSK crystals. Our study elucidated the coupling between the organic

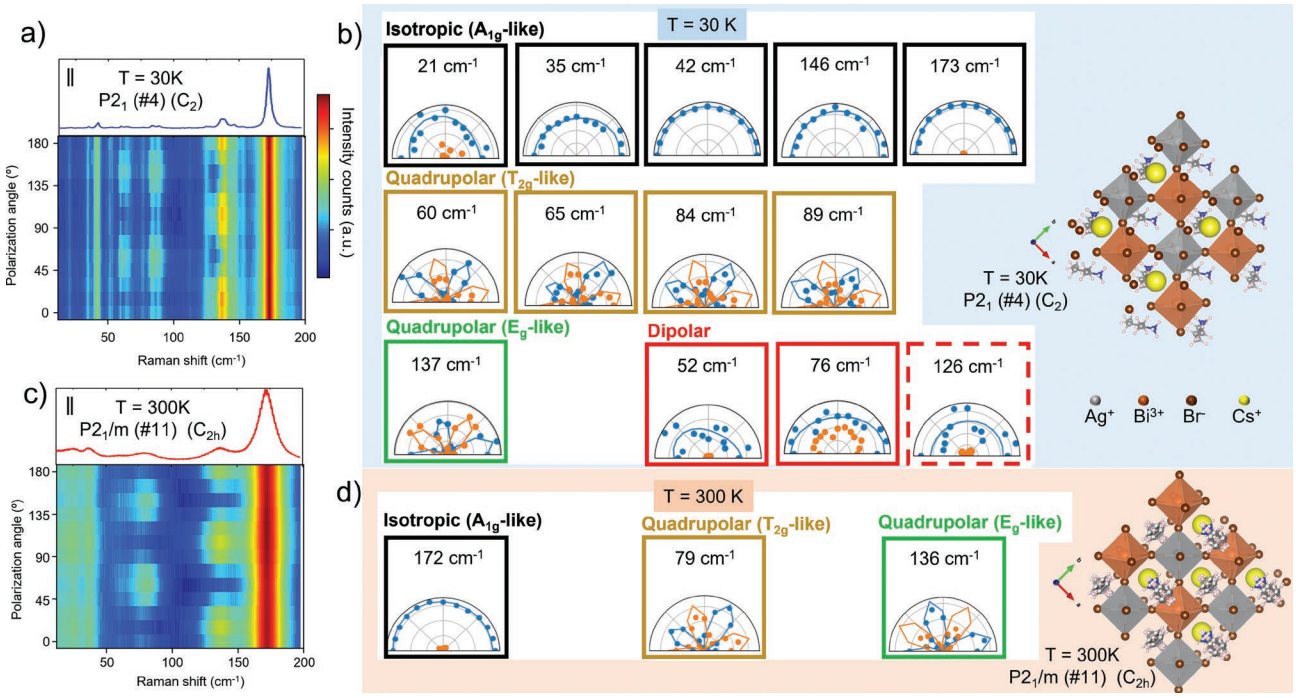

Figure 5. Angle dependence of the phonon modes of the 2L-BA sample: a,c) Color plots of the polarized angle-dependent Raman spectra recorded at 30 and 300 K, respectively (see Figure S5, Supporting Information for angle-dependent Raman spectra in depolarized configuration). b,d) Polar plots of the Raman mode intensities (dots) extracted from the data in Figure 5a,b and Figure S5, Supporting Information, and best fits (lines) obtained from the corresponding Raman tensor equations. Polarized data is shown in blue, depolarized in orange. The top views on the crystal structures of the 2L sample at 30 and 300 K using VESTA software[44] are also shown. The orientation of the principal axes in the octahedra plane is the same as in the polar plots.

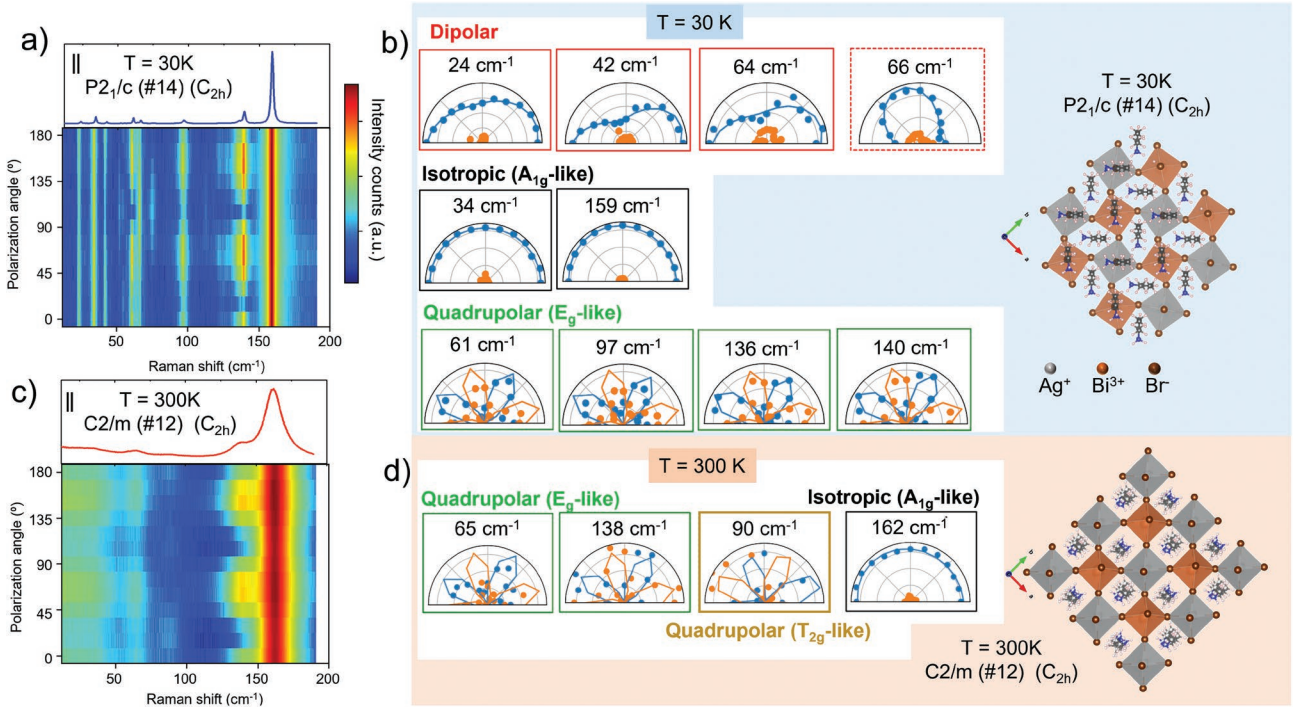

Figure 6. Angle dependence of the phonon modes of the 1L-BA sample: a,c) Color plots of polarization-dependent Raman spectra at 30 and 300 K, respectively (see Figure S6, Supporting Information for angle-dependent Raman spectra in depolarized configuration). b,d) Polar plots of the Raman mode intensities (dots) extracted from the data in Figure 6a,b and Figure S6, Supporting Information, and best fits (lines) obtained from the corresponding Raman tensor equations. Polarized data is shown in blue, depolarized in orange. The top views on the crystal structures of the 1L sample at 30 and 300 K using VESTA software[44] are also displayed. The orientation of the principal axes in the octahedra plane is the same as for the polar plots.

Table 1. Main low-frequency (<200 cm^{-1}) Raman peaks observed for the $Cs_2AgBiBr_6$ crystal, $(BA)_2CsAgBiBr_7$ 2L flakes, and $(BA)_4AgBiBr_8$ 1L flakes at low (30 K) and room temperature (300 K) with the corresponding crystal structures, symmetry, and the correlation among the experimentally observed vibrational modes and angular patterns (I, isotropic; Q, quadrupolar; and D, dipolar) (see Supporting Information for more details).

3D (Tetragonal I4/m, #87) (30 K)			2L-BA (Monoclinic $P2_1$, #4) (30 K)			1L-BA (Monoclinic $P2_1/c$, #14) (30 K)		
Exp. Raman shift [cm^{-1}]	Angular pattern	Symmetry	Exp. Raman shift [cm^{-1}]	Angular pattern	Symmetry	Exp. Raman shift [cm^{-1}]	Angular pattern	Symmetry
29	D	E_g	21	I	A	24	D	A_g
40	Q	B_g	35	I	A	34	I	A_g
45	D	B_g	42	I	A	42	D	A_g
			65	Q	A	61	Q	A_g
73	Q	E_g						
			84	Q	A			
			89	Q	A			
						97	Q	A_g
140	Q	B_g	137	Q	A	140	Q	A_g
180	I	A_g	172	I	A	159	I	A_g
3D (Cubic Fm-3m, #225) (300 K)			2L-BA (Monoclinic $P2_1/m$, #11) (300 K)			1L-BA (Monoclinic C2/m, #12) (300 K)		
Exp. Raman shift [cm^{-1}]	Angular pattern	Symmetry	Exp. Raman shift [cm^{-1}]	Angular pattern	Symmetry	Exp. Raman shift [cm^{-1}]	Angular pattern	Symmetry
			31	I	A_g			
39	Q	T_{2g}	38	I	A_g	35	I	A_g
			62	Q	A_g	65	D	A_g
75	Q	T_{2g}	79	Q	A_g			
						90	Q	A_g
135	Q	E_g	136	Q	A_g	138	Q	A_g
175	I	A_{1g}	172	I	A_g	162	I	A_g

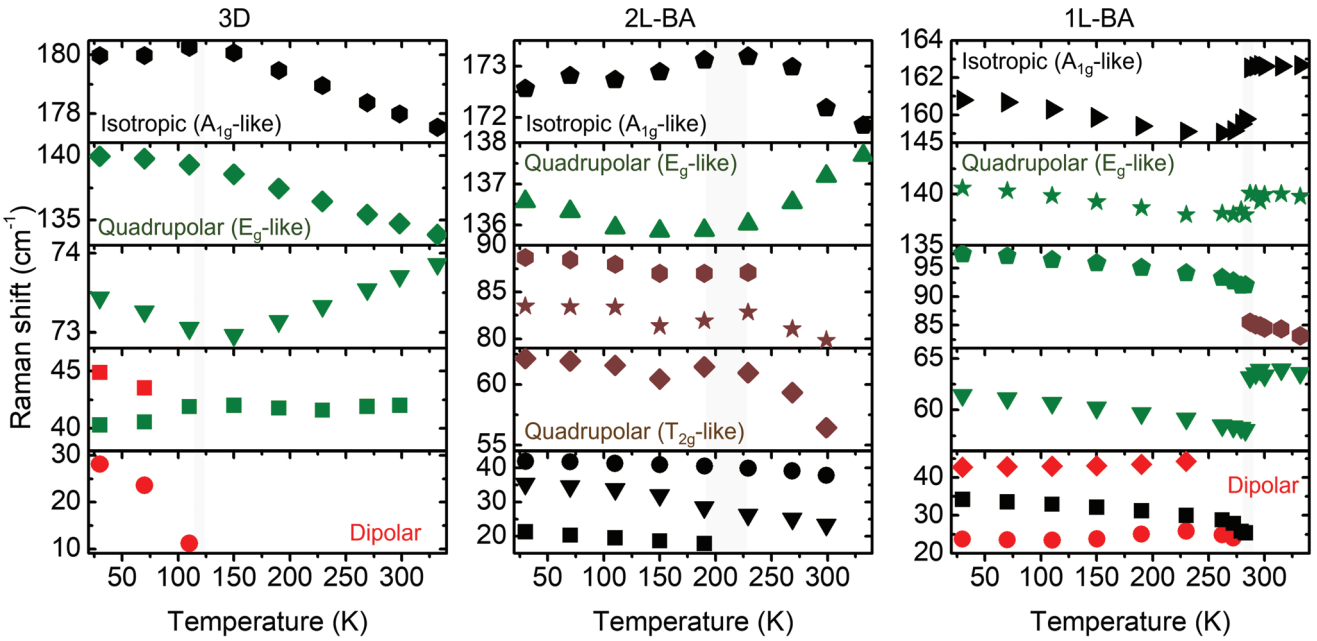

Figure 7. Temperature dependence of the Raman shift of the dominant Raman modes for the 3D crystal and 2L-BA and 1L-BA flakes. The data was collected from the polarized (∥) and depolarized (⊥) configurations.

cations and the inorganic octahedra in the layered structures, and revealed the sensitivity of the low-frequency modes to the phase transitions of the crystal lattice. In this respect, we discovered a secondary phase transition that is determined by the rearrangement of the organic cations coupled to the octahedra layer and which shifts to higher temperature with the reduction of the number of octahedral layers. Therefore, our work provides highly interesting information regarding the temperature-dependent phase transitions in metal-halide PSKs. We show that both the frequency and the symmetry of the phonon mode can be affected by the phase transition, which provides detailed insights into the nature of the phase transition, that is, if it is first or second order, and the properties of the affected phonon mode can also elucidate what processes trigger such transitions.

The insights we gained are highly valuable to understand thermal and optoelectronic properties of such materials. For example, light emission is strongly affected by electron–phonon coupling in this family of double PSK, caused by the extremely flat dispersion of the conduction band edge.[33] This leads to a strong influence of the lattice distortions and phonon coupling on the emission wavelength, and indeed, for 3D PSK and 2L structures the bandgap is indirect and red light emission is caused by radiative defects, while for 1L structures the bandgap is direct around 3 eV, leading to deep blue light emission. Interestingly, the photoluminescence spectra of the 1L samples feature weaker broad emission bands in the visible spectral range, which resemble the self-trapped exciton (STE) emission that is well known for lead halide layered PSKs. STE emission is strongly related to electron–phonon coupling, and our study indicates that similar coupling mechanism should be at work in the double PSKs. This knowledge opens the way to design lead-free materials for white light emission.

Supporting Information

Supporting Information is available from the Wiley Online Library or from the author.

Acknowledgements

B.M-G. and D.S. contributed equally to this work. This work was supported by the Spanish MICINN under Project PID2019-108153GA-I00 and under the María de Maeztu Units of Excellence Programme (MDM-2016-0618). B.M-G. thanks the Gipuzkoa Council (Spain) in the frame of Gipuzkoa Fellows Program and Prof. A. Mateo-Alonso (Molecular and Supramolecular Materials Group – POLYMAT) for the access to the Chemistry Lab to grow the crystals. P.-H.T. and M.-L.L. acknowledge support from the National Natural Science Foundation of China (grant no. 12004377), and R.K. acknowledges the AI-4-QD project financed by the Italian Ministry of Foreign Affairs and International Cooperation (MAECI) within the bilateral Italy–Israel program.

Open Access Funding provided by Istituto Italiano di Tecnologia within the CRUI-CARE Agreement.

Conflict of Interest

The authors declare no conflict of interest.

Data Availability Statement

The data that support the findings of this study are available from the corresponding author upon reasonable request.

Keywords

anisotropy, double perovskites, layered metal-halide perovskites, phase transitions, polarized Raman spectroscopy, vibrational modes

Received: February 1, 2022
Revised: April 11, 2022
Published online: June 9, 2022

[1] B. Vargas, G. RodrÍguez-López, D. Solis-Ibarra, *ACS Energy Lett.* **2020**, *5*, 3591.
[2] H. Lei, D. Hardy, F. Gao, *Adv. Funct. Mater.* **2021**, *31*, 2105898.
[3] E. Greul, M. L. Petrus, A. Binek, P. Docampo, T. Bein, *J. Mater. Chem. A* **2017**, *5*, 19972.
[4] M. Wang, P. Zeng, S. Bai, J. Gu, F. Li, Z. Yang, M. Liu, *Sol. RRL* **2018**, *2*, 1800217.
[5] M. Pantaler, K. T. Cho, V. I. E. Queloz, I. G. Benito, C. Fettkenhauer, I. Anusca, M. K. Nazeeruddin, D. C. Lupascu, G. Grancini, *ACS Energy Lett.* **2018**, *3*, 1781.
[6] F. Igbari, R. Wang, Z.-K. Wang, X.-J. Ma, Q. Wang, K.-L. Wang, Y. Zhang, L.-S. Liao, Y. Yang, *Nano Lett.* **2019**, *19*, 2066.
[7] Z. Zhang, C. Wu, D. Wang, G. Liu, Q. Zhang, W. Luo, X. Qi, X. Guo, Y. Zhang, Y. Lao, B. Qu, L. Xiao, Z. Chen, *Org. Electron.* **2019**, *74*, 204.
[8] C. Wu, Q. Zhang, Y. Liu, W. Luo, X. Guo, Z. Huang, H. Ting, W. Sun, X. Zhong, S. Wei, S. Wang, Z. Chen, L. Xiao, *Adv. Sci.* **2018**, *5*, 1700759.
[9] X. Yang, W. Wang, R. Ran, W. Zhou, Z. Shao, *Energy Fuels* **2020**, *34*, 10513.
[10] J. Yang, C. Bao, W. Ning, B. Wu, F. Ji, Z. Yan, Y. Tao, J. Liu, T. C. Sum, S. Bai, J. Wang, W. Huang, W. Zhang, F. Gao, *Adv. Opt. Mater.* **2019**, *7*, 1801732.
[11] F. Fang, H. Li, S. Fang, B. Zhou, F. Huang, C. Ma, Y. Wan, S. Jiang, Y. Wang, B. Tian, Y. Shi, *Adv. Opt. Mater.* **2021**, *9*, 2001930.
[12] W. Pan, H. Wu, J. Luo, Z. Deng, C. Ge, C. Chen, X. Jiang, W.-J. Yin, G. Niu, L. Zhu, L. Yin, Y. Zhou, Q. Xie, X. Ke, M. Sui, J. Tang, *Nat. Photonics* **2017**, *11*, 726.
[13] X. Cheng, W. Qian, J. Wang, C. Yu, J. He, H. Li, Q. Xu, D. Chen, N. Li, J. Lu, *Small* **2019**, *15*, 1905731.
[14] Z. Liu, H. Yang, J. Wang, Y. Yuan, K. Hills-Kimball, T. Cai, P. Wang, A. Tang, O. Chen, *Nano Lett.* **2021**, *21*, 1620.
[15] B. A. Connor, L. Leppert, M. D. Smith, J. B. Neaton, H. I. Karunadasa, *J. Am. Chem. Soc.* **2018**, *140*, 5235.
[16] L. Mao, S. M. L. Teicher, C. C. Stoumpos, R. M. Kennard, R. A. DeCrescent, G. Wu, J. A. Schuller, M. L. Chabinyc, A. K. Cheetham, R. Seshadri, *J. Am. Chem. Soc.* **2019**, *141*, 19099.
[17] Y. Fang, L. Zhang, L. Wu, J. Yan, Y. Lin, K. Wang, W. L. Mao, B. Zou, *Angew. Chem., Int. Ed.* **2019**, *58*, 15249.
[18] E. T. McClure, A. P. McCormick, P. M. Woodward, *Inorg. Chem.* **2020**, *59*, 6010.
[19] F. Schmitz, J. Horn, N. Dengo, A. E. Sedykh, J. Becker, E. Maiworm, P. Bélteky, Á. Kukovecz, S. Gross, F. Lamberti, K. Müller-Buschbaum, D. Schlettwein, D. Meggiolaro, M. Righetto, T. Gatti, *Chem. Mater.* **2021**, *33*, 4688.
[20] S.-Y. Kim, J.-M. Yang, S.-H. Lee, N.-G. Park, *Nanoscale* **2021**, *13*, 12475.

[21] Z. Xu, X. Liu, Y. Li, X. Liu, T. Yang, C. Ji, S. Han, Y. Xu, J. Luo, Z. Sun, *Angew. Chem., Int. Ed.* **2019**, *58*, 15757.
[22] W. Guo, X. Liu, S. Han, Y. Liu, Z. Xu, M. Hong, J. Luo, Z. Sun, *Angew. Chem.* **2020**, *132*, 13983.
[23] W. Zhang, M. Hong, J. Luo, *Angew. Chem., Int. Ed.* **2020**, *59*, 9305.
[24] Y. Li, T. Yang, Z. Xu, X. Liu, X. Huang, S. Han, Y. Liu, M. Li, J. Luo, Z. Sun, *Angew. Chem., Int. Ed.* **2020**, *59*, 3429.
[25] S. J. Zelewski, J. M. Urban, A. Surrente, D. K. Maude, A. Kuc, L. Schade, R. D. Johnson, M. Dollmann, P. K. Nayak, H. J. Snaith, P. Radaelli, R. Kudrawiec, R. J. Nicholas, P. Plochocka, M. Baranowski, *J. Mater. Chem. C* **2019**, *7*, 8350.
[26] L. Schade, A. D. Wright, R. D. Johnson, M. Dollmann, B. Wenger, P. K. Nayak, D. Prabhakaran, L. M. Herz, R. Nicholas, H. J. Snaith, P. G. Radaelli, *ACS Energy Lett.* **2019**, *4*, 299.
[27] J. Su, T. Mou, J. Wen, B. Wang, *J. Phys. Chem. C* **2020**, *124*, 5371.
[28] A. Schmitz, L. L. Schaberg, S. Sirotinskaya, M. Pantaler, D. C. Lupascu, N. Benson, G. Bacher, *ACS Energy Lett.* **2020**, *5*, 559.
[29] A. Dey, A. F. Richter, T. Debnath, H. Huang, L. Polavarapu, J. Feldmann, *ACS Nano* **2020**, *14*, 5855.
[30] J. A. Steele, P. Puech, M. Keshavarz, R. Yang, S. Banerjee, E. Debroye, C. W. Kim, H. Yuan, N. H. Heo, J. Vanacken, A. Walsh, J. Hofkens, M. B. J. Roeffaers, *ACS Nano* **2018**, *12*, 8081.
[31] A. H. Slavney, T. Hu, A. M. Lindenberg, H. I. Karunadasa, *J. Am. Chem. Soc.* **2016**, *138*, 2138.
[32] P. Pistor, M. Meyns, M. Guc, H.-C. Wang, M. A. L. Marques, X. Alcobé, A. Cabot, V. Izquierdo-Roca, *Scr. Mater.* **2020**, *184*, 24.
[33] B. Martín-García, D. Spirito, G. Biffi, S. Artyukhin, F. Bonaccorso, R. Krahne, *J. Phys. Chem. Lett.* **2021**, *12*, 280.
[34] C. Quarti, G. Grancini, E. Mosconi, P. Bruno, J. M. Ball, M. M. Lee, H. J. Snaith, A. Petrozza, F. De Angelis, *J. Phys. Chem. Lett.* **2014**, *5*, 279.
[35] A. M. A. Leguy, A. R. Goñi, J. M. Frost, J. Skelton, F. Brivio, X. Rodríguez-Martínez, O. J. Weber, A. Pallipurath, M. I. Alonso, M. Campoy-Quiles, M. T. Weller, J. Nelson, A. Walsh, P. R. F. Barnes, *Phys. Chem. Chem. Phys.* **2016**, *18*, 27051.
[36] T. Yin, Y. Fang, X. Fan, B. Zhang, J.-L. Kuo, T. J. White, G. M. Chow, J. Yan, Z. X. Shen, *Chem. Mater.* **2017**, *29*, 5974.
[37] Y. Guo, O. Yaffe, D. W. Paley, A. N. Beecher, T. D. Hull, G. Szpak, J. S. Owen, L. E. Brus, M. A. Pimenta, *Phys. Rev. Mater.* **2017**, *1*, 042401.
[38] J. Ibaceta-Jaña, R. Muydinov, P. Rosado, H. Mirhosseini, M. Chugh, O. Nazarenko, D. N. Dirin, D. Heinrich, M. R. Wagner, T. D. Kühne, B. Szyszka, M. V. Kovalenko, A. Hoffmann, *Phys. Chem. Chem. Phys.* **2020**, *22*, 5604.
[39] C. M. Mauck, A. France-Lanord, A. C. Hernandez Oendra, N. S. Dahod, J. C. Grossman, W. A. Tisdale, *J. Phys. Chem. C* **2019**, *123*, 27904.
[40] N. S. Dahod, A. France-Lanord, W. Paritmongkol, J. C. Grossman, W. A. Tisdale, *J. Chem. Phys.* **2020**, *153*, 044710.
[41] B. Dhanabalan, Y.-C. Leng, G. Biffi, M.-L. Lin, P.-H. Tan, I. Infante, L. Manna, M. P. Arciniegas, R. Krahne, *ACS Nano* **2020**, *14*, 4689.
[42] M. Menahem, Z. Dai, S. Aharon, R. Sharma, M. Asher, Y. Diskin-Posner, R. Korobko, A. M. Rappe, O. Yaffe, *ACS Nano* **2021**, *15*, 10153.
[43] M.-L. Lin, B. Dhanabalan, G. Biffi, Y.-C. Leng, S. Kutkan, M. P. Arciniegas, P.-H. Tan, R. Krahne, *Small* **2022**, *18*, e2106759.
[44] K. Momma, F. Izumi, *J. Appl. Crystallogr.* **2011**, *44*, 1272.
[45] M. A. Pérez-Osorio, Q. Lin, R. T. Phillips, R. L. Milot, L. M. Herz, M. B. Johnston, F. Giustino, *J. Phys. Chem. C* **2018**, *122*, 21703.
[46] X.-L. Liu, X. Zhang, M.-L. Lin, P.-H. Tan, *Chin. Phys. B* **2017**, *26*, 067802.
[47] B. Dhanabalan, G. Biffi, A. Moliterni, V. Olieric, C. Giannini, G. Saleh, L. Ponet, M. Prato, M. Imran, L. Manna, R. Krahne, S. Artyukhin, M. P. Arciniegas, *Adv. Mater.* **2021**, *33*, 2008004.
[48] X. Gong, O. Voznyy, A. Jain, W. Liu, R. Sabatini, Z. Piontkowski, G. Walters, G. Bappi, S. Nokhrin, O. Bushuyev, M. Yuan, R. Comin, D. McCamant, S. O. Kelley, E. H. Sargent, *Nat. Mater.* **2018**, *17*, 550.